

2D FeOCl: A Highly In-Plane Anisotropic Antiferromagnetic Semiconductor Synthesized via Temperature-Oscillation Chemical Vapor Transport

Yi Zeng, Pingfan Gu, Zijing Zhao, Biao Zhang, Zhongchong Lin, Yuxuan Peng, Wei Li, Wanting Zhao, Yuchen Leng, Pingheng Tan, Teng Yang, Zhidong Zhang, Youting Song, Jinbo Yang, Yu Ye, Kesong Tian,* and Yanglong Hou*

2D van der Waals (vdW) transition-metal oxyhalides with low symmetry, novel magnetism, and good stability provide a versatile platform for conducting fundamental research and developing spintronics. Antiferromagnetic FeOCl has attracted significant interest owing to its unique semiconductor properties and relatively high Néel temperature. Herein, good-quality centimeter-scale FeOCl single crystals are controllably synthesized using the universal temperature-oscillation chemical vapor transport (TO-CVT) method. The crystal structure, bandgap, and anisotropic behavior of the 2D FeOCl are explored in detail. The absorption spectrum and electrical measurements reveal that 2D FeOCl is a semiconductor with an optical bandgap of ≈ 2.1 eV and a resistivity of $\approx 10^{-1} \Omega \text{ m}$ at 295 K, and the bandgap increases with decreasing thickness. Strong in-plane optical and electrical anisotropies are observed in 2D FeOCl flakes, and the maximum resistance anisotropic ratio reaches 2.66 at 295 K. Additionally, the lattice vibration modes are studied through temperature-dependent Raman spectra and first-principles density functional calculations. A significant decrease in the Raman frequencies below the Néel temperature is observed, which results from the strong spin–phonon coupling effect in 2D FeOCl. This study provides a high-quality low-symmetry vdW magnetic candidate for miniaturized spintronics.

netic layered transition-metal oxyhalides in a low-symmetry orthorhombic structure provide a new degree of freedom to modulate magnetism,^[3] increasing the attention to explore their low-dimensional properties.^[4–6] Recently, magnetic superstructures and optical anisotropies have been explored in layered single-crystal CrOCl.^[4] Additionally, the atomic structure, work function, and magnetism of VOCl have been investigated.^[5] Interestingly, relatively high Néel temperatures in monolayer FeOX (X = F, Cl, Br, or I) have recently been predicted by theoretical calculations, indicating that they are robust antiferromagnets.^[7]

Bulk FeOCl was first synthesized by Goldsztaub in 1935^[8] and it was reported to have the highest Néel temperature of 92 K among transition-metal oxyhalides.^[4,5,9,10] It has been widely studied, specifically for its structure,^[8,11,12] intercalation,^[13–17] magnetism,^[6,9,12,18] phase transition,^[18,19] and catalytic performance.^[20–23]


Over the past decade, various methods, including chemical vapor transport (CVT),^[8,11–21,24–26] chemical vapor deposition,^[27] partial pyrolysis,^[22,23,28] liquid exfoliation,^[29] chemical exfoliation,^[6] and rapid thermal annealing, have been developed to

1. Introduction

Recently, the dimensional effect of 2D van der Waals (vdW) materials has attracted widespread interest.^[1,2] Antiferromag-

Y. Zeng, Z. Zhao, B. Zhang, W. Li, W. Zhao, K. Tian, Y. Hou
School of Materials Science and Engineering
Beijing Key Laboratory for Magnetoelectric Materials and Devices
Beijing Innovation Centre for Engineering Science and Advanced
Technology
Peking University
Beijing 100871, China
E-mail: tks@pku.edu.cn; hou@pku.edu.cn
P. Gu, Z. Lin, Y. Peng, J. Yang, Y. Ye
State Key Laboratory for Artificial Microstructure and Mesoscopic
Physics
School of Physics
Peking University
Beijing 100871, China

Y. Leng, P. Tan
State Key Laboratory of Superlattices and Microstructures
Institute of Semiconductors
Chinese Academy of Sciences
Beijing 100083, China
T. Yang, Z. Zhang
Shenyang National Laboratory for Materials Science
Institute of Metal Research
Chinese Academy of Sciences
Shenyang 110016, China
Y. Song
Institute of Physics
Chinese Academy of Sciences
Beijing 100190, China

 The ORCID identification number(s) for the author(s) of this article can be found under <https://doi.org/10.1002/adma.202108847>.

DOI: 10.1002/adma.202108847

obtain bulk or few-layer FeOCl.^[30] However, the reported characteristics of bulk FeOCl dispersed using the conventional CVT method with similar growth parameters, including morphology, crystallinity, size, and electrical resistivity (Tables S1 and S2, Supporting Information), and the optical bandgap as well as Raman spectra of FeOCl are still inconclusive (Tables S3 and S4, Supporting Information). Combining CVT and mechanical exfoliation is considered the best method to obtain intrinsically highly crystalline bulk and few-layer FeOCl. Therefore, it is crucial to develop a stable and controllable method for obtaining high-quality FeOCl single crystals and to explore the intrinsic properties and related applications of few-layer FeOCl.

In this study, we successfully synthesized good-quality centimeter-scale FeOCl single crystals by developing a temperature-oscillation chemical vapor transport (TO-CVT) method and conducted a comprehensive study on its properties in the 2D limit. The quality of the obtained single crystals was systematically characterized via X-ray diffraction (XRD), high-resolution transmission electron microscopy (HRTEM), X-ray photoelectron spectroscopy (XPS), Raman spectroscopy, magnetism, and heat-capacity measurements. FeOCl crystals exhibit good air stability and they can be easily exfoliated. The layer-dependent

optical and electrical results indicated the semiconducting characteristics of the 2D FeOCl flakes. We systematically studied the optical and electrical anisotropies of exfoliated FeOCl flakes using angle-dependent polarized Raman spectroscopy and angle-dependent conductivity measurements. In addition, three Raman peaks were observed and identified as A_g modes through calculations and polarized Raman spectra, of which A_g^1 and A_g^2 diverge from the standard anharmonic model below the Néel temperature, revealing strong spin-phonon coupling in 2D FeOCl. Our study on the controllable synthesis of good-quality centimeter-scale FeOCl opens a new opportunity to investigate low-symmetry vdW 2D magnetism and spintronic devices.

2. Results and Discussion

Good-quality single crystals can be obtained by modifying the CVT parameters.^[31,32] Figure 1a schematically illustrates the TO-CVT method for the synthesis of FeOCl, and the temperature settings of the source and sink zones (see details in the Experimental Section) are shown in Figure 1b. The TO-CVT

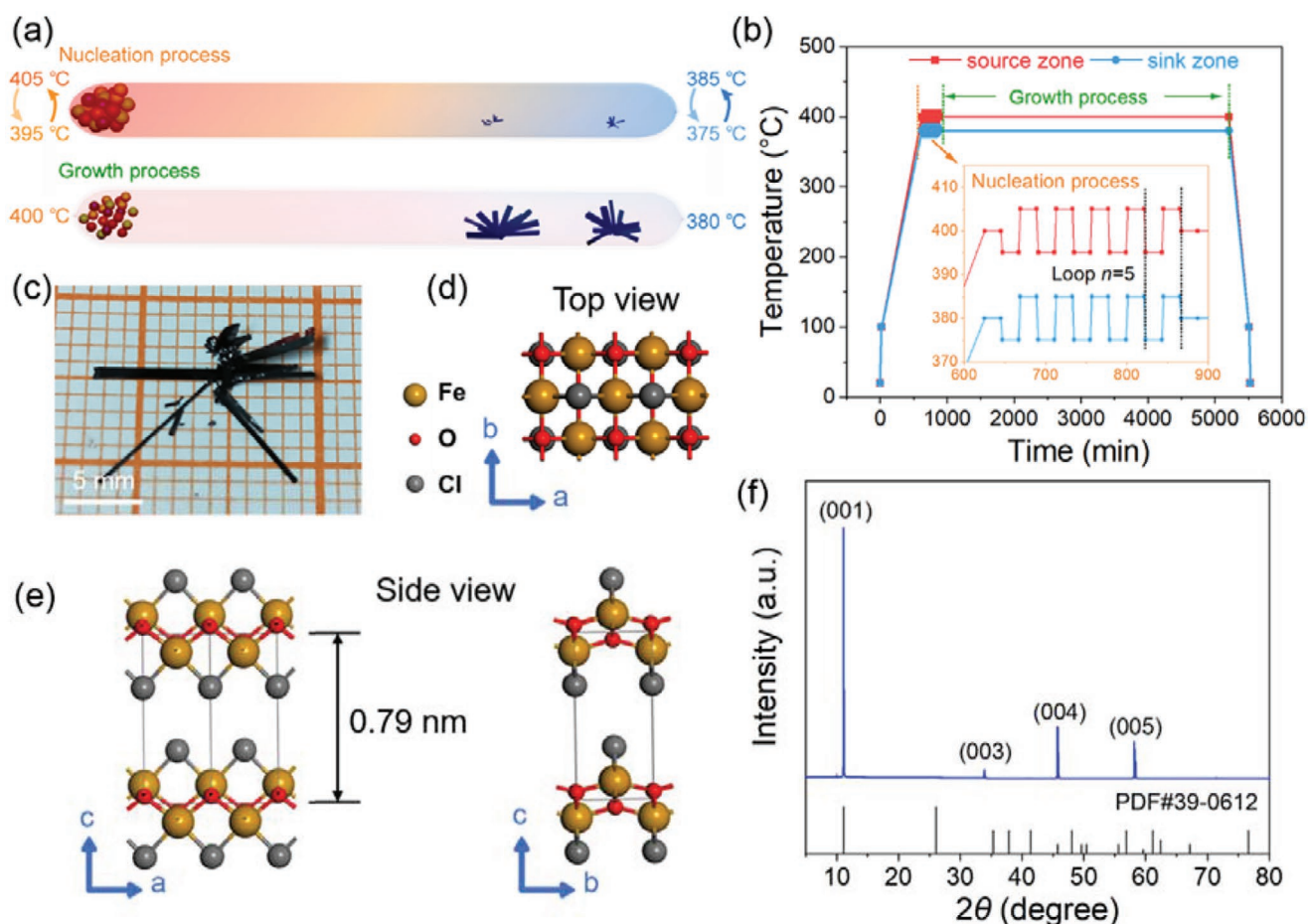


Figure 1. Synthesis schematic and crystal structure of vdW FeOCl. a) Schematic illustration of TO-CVT method, including the nucleation and growth processes. b) Schematic diagram for source and sink zones temperature settings, n is the number of oscillations. c) Photograph of a typical synthesized centimeter single-crystal FeOCl on a grid paper. d) Atomic model of FeOCl viewed from the top. e) Atomic model of FeOCl viewed from the side.^[11] f) XRD pattern of FeOCl single crystal, the observed sharp (00l) peaks imply the good quality of FeOCl single crystal.

method is divided into two steps: nucleation and growth. Controlling the temperature oscillation during nucleation and the growth time during growth are crucial. During nucleation, controlling the temperature oscillation breaks the equilibrium of the gas-solid reversible chemical reaction, which promotes the volatilization of the precursor and the crystallization of the sink zone, accelerating the flow in the ampule at the same time.^[32] During growth, extending the growth time promotes the crystal growth. Compared with the conventional CVT method,^[14,15,17,25] the additional nucleation process improves the nucleation and crystallinity of the crystals. When grown under a static temperature gradient (400/380 °C), there were almost no crystals, but some polycrystalline powders were observed in the sink zone (Figure S1, Supporting Information). Using the TO-CVT method, we obtained FeOCl crystals with metallic black/purple luster and lateral sizes of up to ≈1.2 cm (Figure 1c), which is almost larger than that of the previously reported FeOCl crystals.^[11,13,33,34] When the growth time was gradually increased from 3 to 9 days, the lateral size of the crystals varied from millimeters to centimeters (Figure S2, Supporting Information). Furthermore, the TO-CVT method is an effective and universal strategy for synthesizing other 2D materials, such as FeBr₂, FeCl₃, VCl₃, and RuCl₃, and the size of the FeBr₂ single crystals reaches 5 mm × 5 mm (Figure S3, Supporting Information).

Bulk FeOCl belongs to orthorhombic space group *Pmmn* (No. 59) with two formula units per unit cell. The lattice parameters are *a* = 3.78, *b* = 3.30, and *c* = 7.92 Å, which features a layered structure (Figure 1d,e).^[11] XRD was used to examine the crystal structure and evaluate the crystallinity. As shown in Figure 1f, several sharp peaks are observed in the XRD pattern, and all the diffraction peaks ($2\theta = 11.05^\circ, 33.92^\circ, 45.78^\circ, \text{ and } 58.24^\circ$)

can be attributed to the (001), (003), (004), and (005) crystal planes of orthorhombic FeOCl (PDF#39-0612),^[35] indicating the highly oriented and crystalline nature of the FeOCl crystals, and the surface of the crystal is the *ab* plane. Owing to their layered structure and small exfoliation energy,^[7] FeOCl flakes were prepared via mechanical exfoliation using Scotch tape, and square-like layered FeOCl flakes with lateral dimensions of up to hundreds of microns were obtained (Figure S4, Supporting Information). TEM measurements were performed on exfoliated flakes to study their crystal microstructure. Figure 2a shows a low-magnification TEM image of the FeOCl flakes on a Cu grid. As shown in Figure 2b, the interplanar length is 0.164 nm, corresponding to the (020) plane of FeOCl. Figure 2c displays the sharp selected-area electron diffraction (SAED) spots and they can be denoted as (020) and (200) planes, reflecting the orthogonal symmetry and high crystallinity of the as-exfoliated 2D FeOCl flakes. Energy-dispersive X-ray spectroscopy (EDX) and XPS were employed to elucidate the elemental composition. As shown in Figure 2d–g, the EDX mappings revealed the homogeneous elemental distribution of Fe, O, and Cl without detectable impurities, and the corresponding EDX spectrum demonstrated strong signals of Fe, O, and Cl (Figure 2h), which is consistent with the expected stoichiometric ratio of FeOCl. The entire XPS survey spectra show that Fe, O, and Cl signals are presented in the as-synthesized FeOCl crystal (Figure S5, Supporting Information), and the major peaks of binding energies of 711.9 and 725.4 eV correspond to Fe 2p_{3/2} and Fe 2p_{1/2}, respectively, along with two shake-up satellite peaks at 718.7 and 731.7 eV,^[36] suggesting that the Fe element in FeOCl presents as the Fe^{III} state.^[37] Figure S5c, Supporting Information, shows that the O 1s spectrum can be fitted to two peaks at

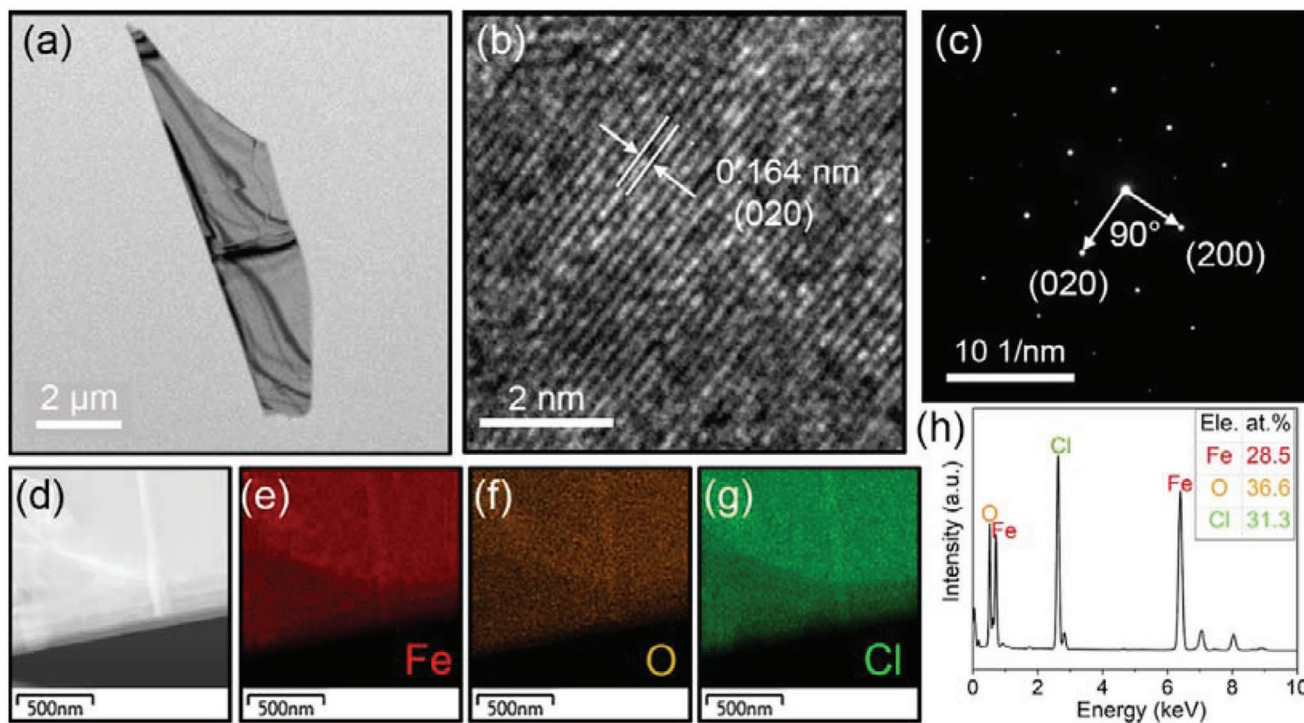


Figure 2. TEM characterization of FeOCl flakes. a) Low-magnification TEM image of the typical FeOCl flake transferred by Scotch tape. b) HRTEM image of the FeOCl flake. c) Corresponding SAED pattern of the FeOCl flake. d–g) EDX mappings of the Fe (e), O (f), and Cl (g). h) EDX spectrum of the flake.

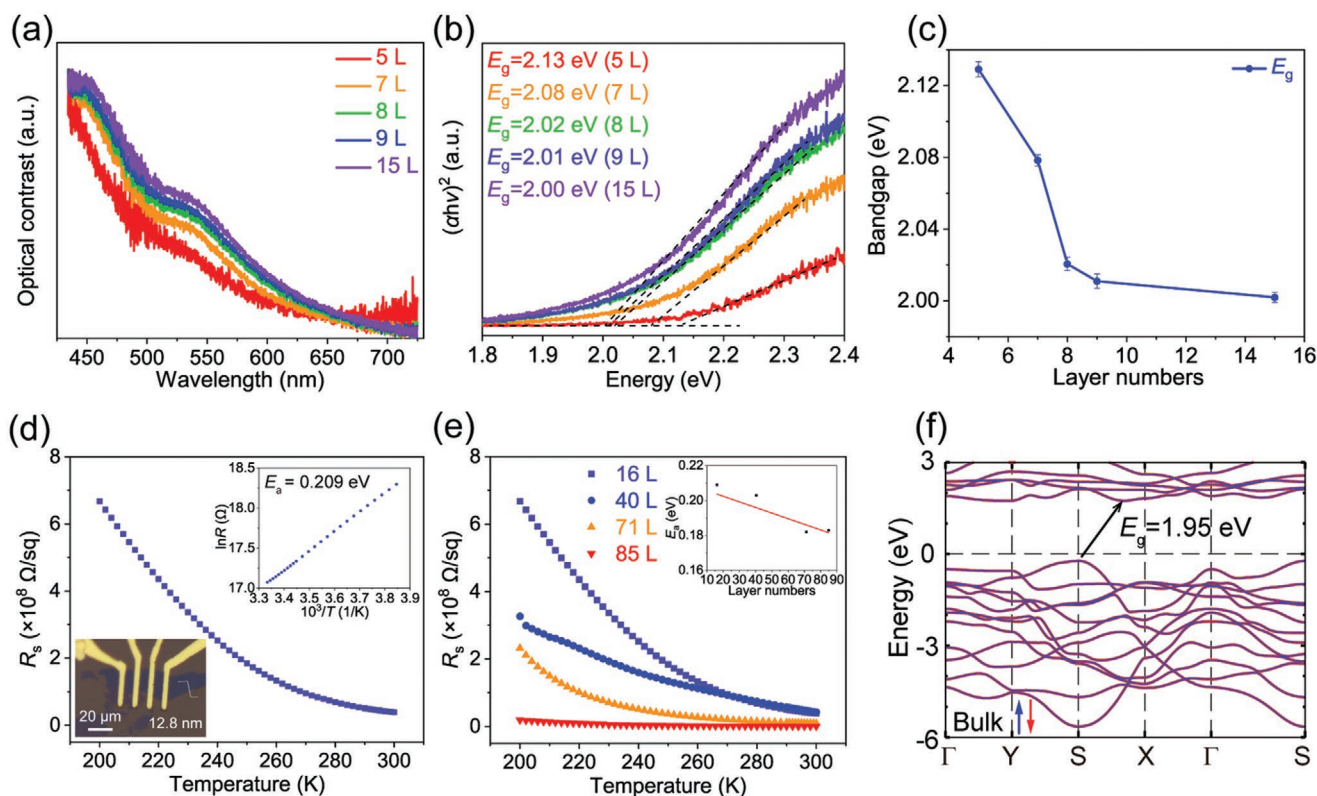


Figure 3. Layer-dependent optical bandgap and electrical properties of FeOCl. a) Optical contrast of multilayer FeOCl flakes. b) $(\alpha h\nu)^2$ plotted versus photon energy $h\nu$ is shown to estimate the optical bandgap, α is the absorption coefficient. c) Layer-dependent optical bandgap obtained from (b). d) R_s of the 12.8 nm FeOCl flake as a function of temperature. Inset: the optical image of the FeOCl device for the R_s - T measurement, the plotted data, and the fitted results using the Arrhenius equation, indicating an activation energy, E_a of 0.209 eV. e) The temperature-dependent sheet resistance curves with the flakes ranging from 16 to 85L. Inset: The activation energy E_a as a function of flake thickness. f) Calculated band structures of bulk FeOCl.

binding energies of 530.4 and 531.6 eV,^[38] corresponding to the lattice oxygen of Fe–O bonds in FeOCl and water molecules adsorbed on the crystal surface.^[22,39] The characteristic peaks with binding energies of 198.7 and 200.3 eV can be attributed to the Cl 2p_{3/2} and Cl 2p_{1/2} peaks, respectively, which is consistent with previous reports.^[22,26,39]

To explore the bandgap of 2D FeOCl flakes with different thicknesses, we conducted optical absorption measurements on FeOCl flakes exfoliated onto a transparent quartz substrate.^[40] We prepared FeOCl flakes of different thicknesses, which were confirmed by atomic force microscopy (AFM) measurements (Figure S6, Supporting Information). Below the absorption edge, two absorption peaks at ≈ 450 and ≈ 525 nm can be observed in the multilayer FeOCl (Figure 3a). The absorbance edges exhibited a blueshift, and the absorption intensities decreased gradually as the thickness decreased. Specific bandgaps were determined from the spectra using Tauc plots, as shown in Figure 3b. When the layers decrease from 15L to 5L, the optical bandgap obviously increases from 2.00 to 2.13 eV (Figure 3c), which are generally larger than the previously reported values for FeOCl.^[22,28,29,41] The successive blueshift of the extracted optical bandgap with the decreasing thickness for 2D FeOCl flakes indicates the enhanced quantum confinement effect in the 2D system.^[42] To investigate the semiconductor properties of the few-layer FeOCl further, electrical measure-

ments were conducted in a 12.8 nm-thick FeOCl flake patterned by standard electron-beam lithography and a lift-off process (Figure 3d), and the sheet resistance (R_s) showed typical semiconducting behavior as the temperature decreased. The resistivity was $5.6 \times 10^{-1} \Omega \text{ m}$ at 295 K, and it increased by an order of magnitude ($\approx 8.5 \Omega \text{ m}$) at 200 K. The activation energy, $E_a = 0.209$ eV, was obtained by fitting the Arrhenius equation of $\ln \rho = \ln \rho_0 + E_a/k_B T$, where k_B is the Boltzmann constant. The change in the activation energy with respect to the layer thickness is shown in the inset of Figure 3e, which corresponds approximately to the layer-dependent bandgap (Figure 3c). These optical and electrical results confirm the semiconducting character of the 2D FeOCl flakes. The semiconducting behavior of FeOCl provides an ideal platform for next-generation low-power ultracompact 2D spintronic devices, such as tunneling magnetoresistance junctions, which can be extended to future research.

To investigate the thickness-dependent band structure of the 2D FeOCl flakes further, band structure calculations were performed using the Vienna Ab initio Simulation Package (VASP).^[7] The calculated band structure of the bulk FeOCl is shown in Figure 3f, and the bandgap varies from 1 to 8 layers of FeOCl flakes, as shown in Figure S7a–h, Supporting Information. The calculated bandgap of FeOCl increased as the number of layers decreased. The experimental and calculation results

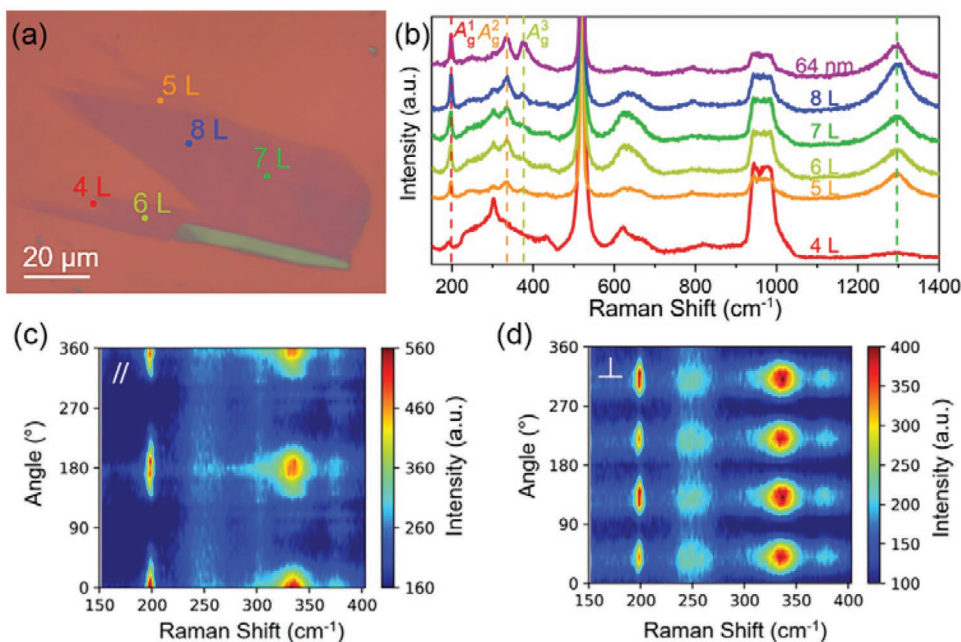


Figure 4. Layer-dependent and angle-dependent polarized Raman spectra of FeOCl flakes. a) Optical image of FeOCl flakes with different layer thicknesses. b) Raman spectra obtained from FeOCl samples ranging from 4L to 64 nm. c,d) Contour color map of normalized Raman intensities under parallel and cross configurations of as-exfoliated FeOCl flake.

both indicated that the bandgap of FeOCl can be engineered by tailoring the number of layers, such as BiOBr and Sb₂Se₃ crystals.^[42,43]

Raman spectroscopy is the most commonly used method for investigating the structure and phonon properties of 2D materials.^[44] Here, we performed layer-dependent and angle-dependent polarized Raman characterizations of the few-layer FeOCl flakes at 295 K. An optical image of the FeOCl flakes is shown in **Figure 4a**, and the corresponding atomic force microscopy (AFM) images are shown in **Figure S8**, Supporting Information. The layer-dependent Raman spectra of FeOCl are shown in **Figure 4b**. In the low-frequency region (150–400 cm⁻¹), three peaks were observed and identified as A_g modes by calculations and polarized Raman spectra. The peak at ≈198.6 cm⁻¹ shows a small redshift as the thickness decreases from 64 nm to 4 layers, whereas those at ≈334.5 and ≈379.7 cm⁻¹ disappear. This could be attributed to the weak intensities of the two vibrational modes in the particular layers.^[45] However, in the high-frequency region (1200–1400 cm⁻¹), the peak at ≈1292.8 cm⁻¹ does not change significantly as the thickness decreases.

To clarify the Raman peaks of FeOCl further (Table S4, Supporting Information), we performed first-principles density functional calculations to study the Raman vibrational modes of FeOCl and their attributions. The calculated Raman spectrum shows that the three Raman-active modes (198.6, 334.5, and 379.7 cm⁻¹) are all A_g modes, as shown in **Figure S9**, Supporting Information, and this can be substantiated by our polarized Raman spectra data. All three modes vibrate along the out-of-plane direction, revealing Fe–O bond rotation (the first two modes) and Fe–Cl bond stretching motion from low to high frequencies, respectively. Moreover, there is one Raman mode at 1292.8 cm⁻¹, which has been reported elsewhere but not assigned.^[23,41] The Raman shift of this mode appears beyond

the highest frequency value in the phonon dispersion relation of FeOCl, suggesting a possible high-order Raman mode, such as the B_{2g} + B_{3u} combination mode from our calculation.

For a quantitative study of the angular dependence of the Raman intensities, various Raman spectra of the FeOCl flakes excited by a 532 nm laser under parallel- and cross-polarization configurations were measured by rotating the sample in the *x*–*y* plane with rotation angles changing from 0° to 360° with a step size of 10°.^[46] The contour color maps of normalized Raman intensities are shown in **Figure 4c,d**. All three A_g modes show clear 180° periodic variations under parallel polarization, and they yield a two-lobed shape with maximum intensities at 0° and 180° (**Figure S10a–c**, Supporting Information). Under cross polarization, all three A_g modes had a period of 90°, which yielded a four-lobed shape with four maximum intensity angles at ≈45°, ≈135°, ≈225°, and ≈315° (**Figure S10d–f**, Supporting Information). The intensity of the dependence of the rotation angle can be well described by the in-plane A_g mode

$$\text{tensor} \begin{pmatrix} |a|e^{i\phi_a} & 0 \\ 0 & |b|e^{i\phi_b} \end{pmatrix}$$

$$I_{\parallel} = |a|^2 (\cos \theta)^4 + |b|^2 (\sin \theta)^4 + 2|a||b| (\cos \theta)^2 (\sin \theta)^2 \cos \varphi_{ab} \quad (1)$$

and

$$I_{\perp} = (|a|^2 + |b|^2 - 2|a||b| \cos \varphi_{ab}) (\cos \theta)^2 (\sin \theta)^2 \quad (2)$$

The extracted matrix elements of the Raman tensors obtained by fitting from Equations (1) and (2) are listed in **Table S5**, Supporting Information. As shown in **Figure S10**, Supporting Information, the axes of these peaks are in the same

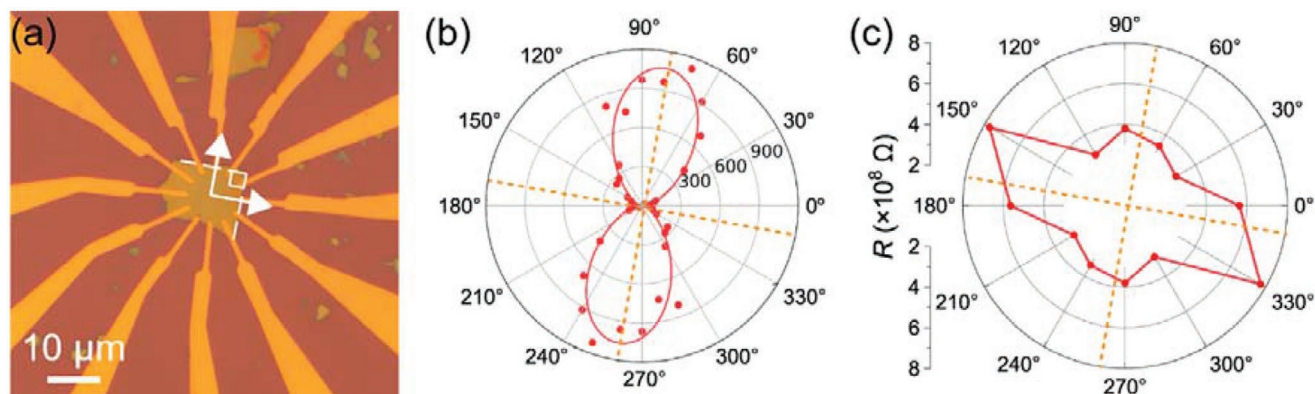


Figure 5. Angle-resolved conductivity of FeOCl flake. a) Optical image of a typical FeOCl flake with 12 electrodes spaced at 30° apart. b) The polarized Raman spectroscopy. c) The polar plot of the angle-resolved conductivity.

direction, indicating that all of these peaks originate from the atomic vibrations of FeOCl.

Temperature-dependent Raman spectroscopy is a powerful technique that perfectly tracks sub-per-centimeter changes to reveal subtle underlying properties.^[47–49] Here, we employed temperature-dependent Raman spectra to study the spin–phonon coupling in 2D FeOCl. The frequencies of the Si and the A_g^3 Raman peaks fit well with the anharmonic model (black dotted line in Figure S12h, Supporting Information), whereas the A_g^1 and A_g^2 Raman peaks of FeOCl exhibit anomalous softening below the Néel temperature, indicating the presence of spin–phonon coupling in FeOCl. As mentioned previously, the A_g^1 and A_g^2 Raman modes of FeOCl are related to the Fe–O bond vibration. The superexchange interactions of the Fe–O–Fe bond determine the spin configuration and phase-transition behavior of FeOCl.^[12] As a result, the A_g^1 and A_g^2 modes are sensitive to magnetic phase transitions and possibly contain information on the magnetic order. The magnetic and heat-capacity measurements provided a consistent Néel temperature of 83.3 K (Figures S13 and S14, Supporting Information), indicating a paramagnetic to antiferromagnetic ordering transition.

In addition to anisotropic optical measurements, the electrical anisotropy of FeOCl was investigated by measuring the angle-resolved conductivity of the FeOCl flake by fabricating 12 electrodes spaced at an angular interval of 30° (Figure 5a). Because of the orthorhombic structure of FeOCl, the flake orientation can be roughly determined by assigning the edges of the rectangular shape to the axis. Additionally, the crystalline orientation was confirmed using polarized Raman spectroscopy (Figure 5b). The I – V curves were measured between each pair of electrodes separated by 180°. As shown in Figure 5c, the measured maximum anisotropic resistance ratio (R_{\max}/R_{\min}) is 2.66 at 295 K, and it can be utilized to design anisotropic electronic devices.

Air stability is the most significant obstacle in the research and application of 2D magnetic materials. We exposed the FeOCl crystals and flakes to the air for 3 months and conducted XRD and Raman measurements (Figures S15 and S16, Supporting Information). There were no noticeable changes between the fresh and stored samples, indicating that FeOCl is stable in air, which makes FeOCl a promising material for future studies of 2D magnetism.

3. Conclusion

We have developed a universal TO-CVT method for the controllable synthesis of good-quality centimeter-scale FeOCl single crystals and investigated its spectroscopic and microscopic properties in the 2D limit. FeOCl single crystals with a low-symmetry orthorhombic structure and strong in-plane anisotropic nature are revealed by various characterizations. The evolution of the thickness-dependent band structure of the 2D FeOCl flakes is explored experimentally and theoretically. In addition, the absorption spectrum and electrical measurements reveal that 2D FeOCl is a semiconductor with an optical bandgap of ≈ 2.1 eV and a resistivity of $\approx 10^{-1}$ Ω m at 295 K. In addition, the lattice and spin–phonon coupling in FeOCl are studied via systematic Raman measurements and calculations. More importantly, bulk and few-layer FeOCl exhibit good air stability after 3 months of storage under an atmospheric condition. This study enriches the low-symmetry vdW magnetic family and facilitates research progress in spintronics.

Supporting Information

Supporting Information is available from the Wiley Online Library or from the author.

Acknowledgements

This work was supported financially by the National Key Research and Development Program of China (Grants 2017YFA0206301 and 2018YFA0306900) and the National Natural Science Foundation of China (Grants 51631001 and 51672010). The authors acknowledge Electron Microscopy Laboratory in Peking University for the use of Cs corrected electron microscope. The authors are grateful for discussions with Z. F. Li and W. H. Wang.

Conflict of Interest

The authors declare no conflict of interest.

Data Availability Statement

The data that support the findings of this study are available from the corresponding author upon reasonable request.

Keywords

2D materials, antiferromagnetic semiconductors, FeOCl, in-plane anisotropy, single crystals, spin–phonon coupling

Received: November 2, 2021

Revised: January 30, 2022

Published online: February 24, 2022

- [1] K. S. Burch, D. Mandrus, J. G. Park, *Nature* **2018**, 563, 47.
- [2] Y. Khan, S. M. Obaidulla, M. R. Habib, A. Gayen, T. Liang, X. F. Wang, M. S. Xu, *Nano Today* **2020**, 34, 100902.
- [3] T. C. Song, X. H. Cai, M. W. Tu, X. Zhang, B. Huang, N. P. Wilson, K. L. Seyler, L. Zhu, T. Taniguchi, K. Watanabe, M. A. McGuire, D. H. Cobden, D. Xiao, W. Yao, X. D. Xu, *Science* **2018**, 360, 1214.
- [4] T. L. Zhang, Y. M. Wang, H. X. Li, F. Zhong, J. Shi, M. H. Wu, Z. Y. Sun, W. F. Shen, B. Wei, W. D. Hu, X. F. Liu, L. Huang, C. G. Hu, Z. C. Wang, C. B. Jiang, S. X. Yang, Q. Zhang, Z. Qu, *ACS Nano* **2019**, 13, 11353.
- [5] W. J. Wang, R. Sun, S. J. He, Z. Y. Jia, C. L. Su, Y. Li, Z. C. Wang, *2D Mater.* **2021**, 8, 015027.
- [6] A. M. Ferrenti, S. Klemenz, S. Lei, X. Song, P. Ganter, B. V. Lotsch, L. M. Schoop, *Inorg. Chem.* **2020**, 59, 1176.
- [7] S. Y. Wang, J. J. Wang, M. Khazaei, *Phys. Chem. Chem. Phys.* **2020**, 22, 11731.
- [8] S. Goldsztaub, *Bull. Soc. Fr. Mineral.* **1935**, 58, 49.
- [9] R. W. Grant, *J. Appl. Phys.* **1971**, 42, 1619.
- [10] S. X. Yang, T. L. Zhang, C. B. Jiang, *Adv. Sci.* **2021**, 8, 2002488.
- [11] M. D. Lind, *Acta Crystallogr. B* **1970**, 26, 1058.
- [12] S. R. Hwang, W. H. Li, K. C. Lee, J. W. Lynn, C. G. Wu, *Phys. Rev. B* **2000**, 62, 14157.
- [13] F. Kanamaru, M. Shimada, M. Koizumi, M. Takano, T. Takada, *J. Solid State Chem.* **1973**, 7, 297.
- [14] S. M. Kauzlarich, B. K. Teo, B. A. Averill, *Inorg. Chem.* **1986**, 25, 1209.
- [15] J. F. Bringley, B. A. Averill, *Chem. Mater.* **1990**, 2, 180.
- [16] C. G. Wu, D. C. Degroot, H. O. Marcy, J. L. Schindler, C. R. Kannewurf, T. Bakas, V. Papaefthymiou, W. Hirpo, J. P. Yesinowski, Y. J. Liu, M. G. Kanatzidis, *J. Am. Chem. Soc.* **1995**, 117, 9229.
- [17] T. T. Yu, X. Y. Zhao, L. Q. Ma, X. D. Shen, *Mater. Res. Bull.* **2017**, 96, 485.
- [18] J. Zhang, A. Wölfel, L. Li, S. V. Smaalen, H. L. Williamson, R. K. Kremer, *Phys. Rev. B* **2012**, 86, 134428.
- [19] M. Bykov, E. Bykova, S. V. Smaalen, L. Dubrovinsky, C. McCammon, V. Prakapenka, H. P. Liermann, *Phys. Rev. B* **2013**, 88, 014110.
- [20] X. J. Yang, X. M. Xu, J. Xu, Y. F. Han, *J. Am. Chem. Soc.* **2013**, 135, 16058.
- [21] A. E. ElMetwally, G. Eshaq, F. Z. Yehia, A. M. Al-Sabagh, S. Kegnaes, *ACS Catal.* **2018**, 8, 10668.
- [22] B. Y. Zhang, M. D. Chen, D. Y. Li, H. M. Xu, D. S. Xia, *J. Photochem. Photobiol. A* **2020**, 386, 112072.
- [23] L. Chen, S. Y. Zuo, Z. Y. Guan, H. M. Xu, D. S. Xia, D. Y. Li, *Res. Chem. Intermed.* **2021**, 47, 795.
- [24] A. Sagua, E. Morán, M. A. Alario-Franco, A. Rivera, C. León, J. Santamaria, J. Sanz, *Int. J. Inorg. Mater.* **2001**, 3, 293.
- [25] Y. D. Dai, Z. Yu, H. B. Huang, Y. He, T. Shao, Y. F. Hsia, *Mater. Chem. Phys.* **2003**, 79, 94.
- [26] J. L. Wang, M. Tsai, Z. Y. Lu, Y. Li, G. T. Huang, H. L. Wang, H. L. Liu, X. Y. Liao, B. Hwang, A. Neumann, X. J. Yang, *ACS Omega* **2019**, 4, 21945.
- [27] C. W. Wang, S. Yang, H. B. Jiang, H. G. Yang, *Chem. - Eur. J.* **2015**, 21, 18024.
- [28] M. D. Chen, H. M. Xu, Q. Wang, D. Y. Li, D. S. Xia, *Chem. Phys. Lett.* **2018**, 706, 415.
- [29] J. Zhang, X. L. Jiao, Y. G. Xia, F. F. Liu, Y. P. Pang, X. F. Zhao, D. R. Chen, *Chem. - Eur. J.* **2016**, 22, 9321.
- [30] J. Zhang, G. D. Liu, P. H. Wang, S. J. Liu, *New J. Chem.* **2017**, 41, 10339.
- [31] S. P. Faile, *J. Cryst. Growth* **1978**, 43, 129.
- [32] Z. F. Li, X. K. Xi, B. Ding, H. Li, E. K. Liu, Y. Yao, W. H. Wang, *Cryst. Growth Des.* **2020**, 20, 706.
- [33] R. S. Bannwart, J. E. Phillips, R. H. Herber, *J. Solid State Chem.* **1987**, 71, 540.
- [34] M. E. Pieczko, J. J. Breen, *Langmuir* **1995**, 11, 1412.
- [35] J. Q. Wu, Y. F. Liu, X. J. Yang, J. L. Wang, J. Yang, *Chin. Chem. Lett.* **2021**, 32, 2503.
- [36] F. C. Zheng, D. Q. Zhu, X. H. Shi, Q. W. Chen, *J. Mater. Chem. A* **2015**, 3, 2815.
- [37] J. Zhang, M. Y. Zhan, L. L. Zheng, C. Zhang, G. D. Liu, J. Q. Sha, S. J. Liu, S. Tian, *Inorg. Chem.* **2019**, 58, 250.
- [38] C. Q. Tan, Q. L. Xu, T. Y. Sheng, X. X. Cui, Z. R. Wu, H. Y. Gao, H. Li, *J. Hazard. Mater.* **2020**, 398, 123084.
- [39] Y. Y. Wang, H. W. Zhang, Y. D. Zhu, Z. F. Dai, H. M. Bao, Y. Wei, W. P. Cai, *Adv. Mater. Interfaces* **2016**, 3, 1500801.
- [40] Y. X. Peng, X. Cheng, P. F. Gu, F. G. Wang, J. Yang, M. Z. Xue, W. Y. Yang, C. S. Wang, S. Q. Liu, K. J. Watanabe, T. Taniguchi, Y. Yu, J. B. Yang, *Adv. Funct. Mater.* **2020**, 30, 1910036.
- [41] J. Zhang, G. Zhang, Q. H. Ji, H. C. Lan, J. H. Qu, H. J. Liu, *Appl. Catal. B* **2020**, 266, 118665.
- [42] M. Zhao, J. W. Su, Y. Zhao, P. Luo, F. K. Wang, W. Han, Y. Li, X. T. Zu, L. Qiao, T. Y. Zhai, *Adv. Funct. Mater.* **2020**, 30, 1909849.
- [43] C. H. Gong, J. W. Chu, S. F. Qian, C. J. Yin, X. Z. Hu, H. B. Wang, Y. Wang, X. Ding, S. C. Jiang, A. Li, Y. P. Gong, X. F. Wang, C. B. Li, T. Y. Zhai, J. Xiong, *Adv. Mater.* **2020**, 32, 1908242.
- [44] D. J. Late, *ACS Appl. Mater. Interfaces* **2015**, 7, 5857.
- [45] P. Yu, Q. S. Zeng, C. Zhu, L. J. Zhou, W. N. Zhao, J. C. Tong, Z. Liu, G. W. Yang, *Adv. Mater.* **2021**, 33, 2005607.
- [46] X. L. Xu, Q. J. Song, H. F. Wang, P. Li, K. Zhang, Y. L. Wang, K. Yuan, Z. C. Yang, Y. Ye, L. Dai, *ACS Appl. Mater. Interfaces* **2017**, 9, 12601.
- [47] Y. Tian, M. Gray, H. W. Ji, R. Cava, K. Burch, *2D Mater.* **2016**, 3, 025035.
- [48] L. J. Du, J. Tang, Y. C. Zhao, X. M. Li, R. Yang, X. R. Hu, X. Y. Bai, X. Wang, K. J. Watanabe, T. Taniguchi, D. X. Shi, G. Q. Yu, X. D. Bai, T. Hasan, G. Y. Zhang, Z. P. Sun, *Adv. Funct. Mater.* **2019**, 29, 1904734.
- [49] D. P. Kozlenko, O. N. Lis, S. E. Kichanov, E. V. Lukin, N. M. Belozeroва, B. N. Savenko, *npj Quantum Mater.* **2021**, 6, 19.